A Comparative Experimental Study of Multi-Tasking Tracking and Interaction Control on a Torque-Controlled Humanoid Robot

Wu, Xuwei and Ott, Christian and Dietrich, Alexander

A Comparative Experimental Study of Multi-Tasking Tracking and Interaction Control on a Torque-Controlled Humanoid Robot

Xuwei Wu, Christian Ott, and Alexander Dietrich

***Abstract*— Multi-tasking control exploits kinematic redundancy of robots to attain several control objectives at the same time. To properly coordinate the subtasks according to their importance, they are usually stacked into a prioritized hierarchy. In this work, two passivity-based multi-tasking control strategies developed in our recent work that feature strict prioritization and mathematically proved stability properties, are experimentally compared with a state-of-the-art method using feedback linearization on a torque-controlled humanoid robot. The conducted experimental study aims at providing insights into the practical properties of the controllers in real-world scenarios whence the robot has to execute a mixture of trajectory tracking and physical interaction tasks.**

I. Introduction

Modern robotic systems with high degrees of freedom (DOF) such as humanoids [1]–[3] can accomplish several tasks simultaneously by using multi-tasking control to exploit the motion redundancy of the underlying high-dimensional operational space. For example, the humanoid robot Justin, as depicted in Fig. 1, can perform household tasks like wiping windows or sweeping the floor with coordinated whole-body motions [4]. Such real-world applications require a multi-tasking control scheme not only to achieve good trajectory tracking accuracy but also to ensure stable and compliant behavior of the robot during physical interaction with the environments/humans.

A basic concept of multi-tasking control is to stack the subtasks in a prioritized manner with either soft or strict hierarchical order. Optimization-based approaches are often used for soft prioritization by assigning different weights to tasks in the quadratic program (QP) formulation [5]–[7]. If any safety-relevant tasks, such as collision avoidance, are to be incorporated into a task hierarchy, the alternative with strict prioritization is usually adopted to prevent lower-priority tasks from disturbing the higher-priority ones. A standard way to implement strict priorities is to apply null-space projection techniques [8], [9], which can inertially decouple task-space dynamics, if the used projectors fulfill the dynamic consistency condition [10]. Within the catalog of multi-tasking control frameworks with strict prioritization, one can generally distinguish between feedback-linearization-based and passivity-based approaches. One of the well-established methods within the former is the operational space formulation (OSF) [11]–[14], which performs full decoupling of closed-loop dynamics via feedback. Hence, it inevitably involves active inertia shaping and requires the feedback of external forces/torques in case of physical interaction with the environment. Theoretically, it features superior exponential stability with configuration-independent convergence rate through pole placement. However, the complete compensation for closed-loop nonlinearities can be brittle in practice due to model uncertainties [14]. Passivity-based methods [15]–[17], on the other hand, intend to reduce decoupling compensation to a minimum extent, i. e. , avoiding inertia shaping while achieving overall asymptotic stability for the regulation case. Recently, the trajectory tracking case has been addressed by the hierarchical PD+ tracking controller (HPD+) in [18], which utilizes hierarchy-consistent feedforward compensation for inertial and Coriolis/centrifugal effects. A formal proof has been conducted to conclude uniform asymptotic stability of the origin. In [19], the HPD+ control scheme has been extended with external force feedback in order to annihilate the remaining cross-couplings at kinematic level and in generalized task-space external forces. As a result, it achieves uniform exponential stability in free motion and input-to-state stability under bounded interaction forces/torques. However, both HPD+ and the so-called passive decoupled multi-task controller (PDMT) proposed in [19] have only been experimentally validated on a 7-DOF robot manipulator, raising questions about their applicability to more complex robotic systems with highly coupled dynamics such as humanoids.

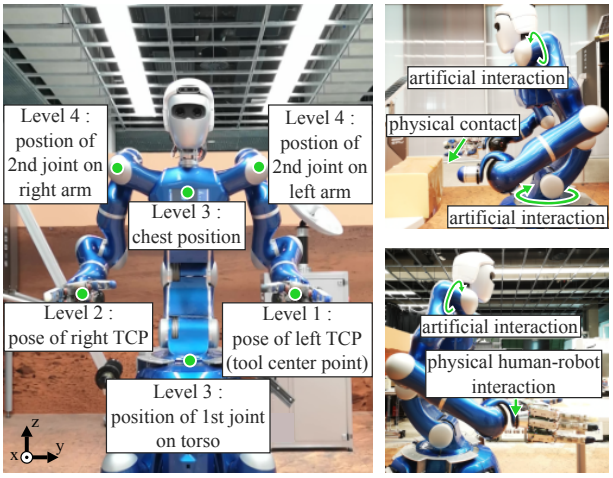

Fig. 1. Experimental setup on Justin. Left: definition of the task hierarchy with four levels. Right: interaction conditions for the experiments.

The main contribution of this work is the comprehensive experimental comparisons of multi-tasking tracking con-

This work is partly supported by the Bavarian Ministry of Economic Affairs, Regional Development and Energy (StMWi) by means of the project SMiLE2gether (LABAY102).

The authors are with the Institute of Robotics and Mechatronics, German Aerospace Center (DLR), 82234 Wessling, Germany. Contact: xuwei.wu@dlr.de.

trollers that feature: 1) a strictly prioritized task hierarchy using null-space projections; 2) mathematically proved stability properties; 3) an impedance control interface for each task to assign desired interactive behavior. More specifically, the practical tracking performance and physical interaction behavior of the classical OSF [12], [13], HPD+, and PDMT are experimentally validated and compared on the humanoid robot Justin. To the best of our knowledge, the considered controllers have never been compared with each other from a combined perspective of tracking and interaction control on the same humanoid platform.

The remainder of this paper is organized as follows: Section II recalls the fundamentals of inertially decoupled task-space dynamics and describes the problem statement. The multi-tasking control methods considered for the comparative study are briefly recapitulated in Section III. Section IV reports and discusses the experimental results. Finally, Section VI concludes the paper.

II. Fundamentals and Problem Statement

A. Upper-Body Dynamics of Justin

The upper body of Justin has 41 actuated DOF with torque control interface[1], including three for the torso, seven for each arm, and twelve for each hand. For the experimental design in this work, the joints of both hands are not considered and remain switched off. The torso also contains one passive joint in the chest which is kinematically coupled with the two preceding actuated joints through tendons. This allows the chest to be kept in an upright position [20].

Taking the kinematic couplings of the torso joints into account, the upper-body dynamics of Justin (excluding the motion of the hands) can be described as a fully-actuated system with $n = 17$ DOF:

$$\boldsymbol{M}(\boldsymbol{q})\ddot{\boldsymbol{q}} + \boldsymbol{C}(\boldsymbol{q},\dot{\boldsymbol{q}})\dot{\boldsymbol{q}} + \boldsymbol{g}(\boldsymbol{q}) = \boldsymbol{\tau} + \boldsymbol{\tau}^{\mathrm{ext}} \ , \tag{1}$$

where $\boldsymbol{q}, \dot{\boldsymbol{q}}, \ddot{\boldsymbol{q}} \in \mathbb{R}^{17}$ denotes the joint positions, velocities, and accelerations, respectively. The symmetric and positive definite inertia matrix is defined by $\boldsymbol{M}(\boldsymbol{q}) \in \mathbb{R}^{17\times 17}$ and the Coriolis/centrifugal matrix by $\boldsymbol{C}(\boldsymbol{q},\dot{\boldsymbol{q}}) \in \mathbb{R}^{17\times 17}$. We assume that $\dot{\boldsymbol{M}}(\boldsymbol{q},\dot{\boldsymbol{q}}) - 2\boldsymbol{C}(\boldsymbol{q},\dot{\boldsymbol{q}})$ is skew-symmetric by choosing a proper form of $\boldsymbol{C}(\boldsymbol{q},\dot{\boldsymbol{q}})$ such as in [21], [22]. The gravitational effects are represented by $\boldsymbol{g}(\boldsymbol{q}) \in \mathbb{R}^{17}$. The motor torques $\boldsymbol{\tau} \in \mathbb{R}^{17}$ and the external torques $\boldsymbol{\tau}^{\mathrm{ext}} \in \mathbb{R}^{17}$ are the inputs to the system.

B. Task Hierarchy and Inertially Decoupled Dynamics

Consider a task hierarchy with $r > 1$ levels, each task can be described by task coordinates and velocities defined as[2]

$$\boldsymbol{x}_i = \boldsymbol{f}_i(\boldsymbol{q}) \in \mathbb{R}^{m_i} \ , \quad \dot{\boldsymbol{x}}_i = \boldsymbol{J}_i(\boldsymbol{q})\dot{\boldsymbol{q}} \tag{2}$$

with the task dimension $m_i < n$. For $i < j \leq r$, the i-th task has a higher priority than the j-th task. All subtask Jacobian matrices $\boldsymbol{J}_i(\boldsymbol{q}) \in \mathbb{R}^{m_i\times n}$ can be stacked as [9]

$$\boldsymbol{J}(\boldsymbol{q}) = \begin{bmatrix}\boldsymbol{J}_1^T(\boldsymbol{q}) & \dots & \boldsymbol{J}_r^T(\boldsymbol{q})\end{bmatrix}^T \in \mathbb{R}^{n\times n} \ . \tag{3}$$

Likewise, all task velocities are hierarchically stacked in the vector $\dot{\boldsymbol{x}} = \boldsymbol{J}(\boldsymbol{q})\dot{\boldsymbol{q}} \in \mathbb{R}^n$. We assume that all tasks are structurally feasible and free of kinematic singularities during execution. Thus, $\boldsymbol{J}(\boldsymbol{q})$ is invertible, and the collocated external forces w. r. t. $\dot{\boldsymbol{x}}$ can be obtained by

$$\boldsymbol{F}_{\dot{\boldsymbol{x}}}^{\mathrm{ext}} = \boldsymbol{J}(\boldsymbol{q})^{-T}\boldsymbol{\tau}^{\mathrm{ext}} = \begin{bmatrix}\boldsymbol{F}_{\dot{\boldsymbol{x}}_1}^{\mathrm{ext},T} & \dots & \boldsymbol{F}_{\dot{\boldsymbol{x}}_r}^{\mathrm{ext},T}\end{bmatrix}^T \ , \tag{4}$$

where $\boldsymbol{F}_{\dot{\boldsymbol{x}}_i}^{\mathrm{ext}} \in \mathbb{R}^{m_i}$ denotes the individual generalized external forces on the i-th hierarchy level.

In the following, dependencies on $\boldsymbol{q}, \dot{\boldsymbol{q}}$ are omitted for the sake of simplicity. In order to implement strict priorities, each $\boldsymbol{J}_i$ is projected onto the null space of all higher level tasks by $\bar{\boldsymbol{J}}_i = \boldsymbol{J}_i\boldsymbol{N}_i^T$. The null-space projectors $\boldsymbol{N}_i \in \mathbb{R}^{n\times n}$ are chosen to be dynamically consistent [10], which can be recursively computed by [13], [23]

$$\boldsymbol{N}_1 = \boldsymbol{I} \ , \quad \bar{\boldsymbol{J}}_1 = \boldsymbol{J}_1 \ , \tag{5a}$$

$$\bar{\boldsymbol{J}}_i^{M+} = \boldsymbol{M}^{-1}\bar{\boldsymbol{J}}_i^T(\bar{\boldsymbol{J}}_i\boldsymbol{M}^{-1}\bar{\boldsymbol{J}}_i^T)^{-1} \ , \tag{5b}$$

$$\boldsymbol{N}_i = \boldsymbol{N}_{i-1} - \bar{\boldsymbol{J}}_{i-1}^T\bar{\boldsymbol{J}}_{i-1}^{M+,T} \ , \tag{5c}$$

in which $\bar{\boldsymbol{J}}_i^{M+}$ represents the dynamically consistent pseudoinverse of $\bar{\boldsymbol{J}}_i$ using the inertia matrix as weight matrix. Similar to (3), the projected Jacobian matrices can be stacked as $\bar{\boldsymbol{J}} = \begin{bmatrix}\bar{\boldsymbol{J}}_1^T & \dots & \bar{\boldsymbol{J}}_r^T\end{bmatrix}^T$ with the inverse given by [17]

$$\bar{\boldsymbol{J}}^{-1} = \begin{bmatrix}\bar{\boldsymbol{J}}_1^{M+} & \dots & \bar{\boldsymbol{J}}_r^{M+}\end{bmatrix} \ . \tag{6}$$

Using the prioritized task coordinates $\boldsymbol{v} = \bar{\boldsymbol{J}}\dot{\boldsymbol{q}}$, one can obtain the inertially decoupled task-space dynamics

$$\boldsymbol{\Lambda}\dot{\boldsymbol{v}} + \boldsymbol{\mu}\boldsymbol{v} = \bar{\boldsymbol{J}}^{-T}(\boldsymbol{\tau} + \boldsymbol{\tau}^{\mathrm{ext}} - \boldsymbol{g}) \ , \tag{7a}$$

$$\boldsymbol{\Lambda} = \bar{\boldsymbol{J}}^{-T}\boldsymbol{M}\bar{\boldsymbol{J}}^{-1} = \mathrm{diag}\{\boldsymbol{\Lambda}_i\} \ , \tag{7b}$$

$$\boldsymbol{\mu} = (\bar{\boldsymbol{J}}^{-T}\boldsymbol{C} - \boldsymbol{\Lambda}\dot{\bar{\boldsymbol{J}}}\,)\bar{\boldsymbol{J}}^{-1} \ , \tag{7c}$$

where $\boldsymbol{\Lambda}, \boldsymbol{\mu} \in \mathbb{R}^{n\times n}$ are the task-space inertia and Coriolis/centrifugal matrices, respectively. The notation $\mathrm{diag}\{\boldsymbol{A}_i\}$ for $i = 1 \dots r$ describes a block diagonal matrix with submatrices $\boldsymbol{A}_i \in \mathbb{R}^{m_i\times m_i}$ located along its diagonal. The subtask inertia $\boldsymbol{\Lambda}_i \in \mathbb{R}^{m_i\times m_i}$ can be individually computed by $(\bar{\boldsymbol{J}}_i\boldsymbol{M}^{-1}\bar{\boldsymbol{J}}_i^T)^{-1}$ [13].

C. Problem Statement

For the comparative study, the considered control methods, as will be shown in Section III, are experimentally evaluated in two application scenarios:

- *Trajectory tracking*: The control objective of each task is to follow a reference trajectory $\boldsymbol{x}_{i,\mathrm{des}}(t) \in \mathbb{R}^{m_i}$ depending on time t, which has continuous and bounded time derivatives $\dot{\boldsymbol{x}}_{i,\mathrm{des}}(t), \ddot{\boldsymbol{x}}_{i,\mathrm{des}}(t)$. The tracking performances of the controllers are compared in terms of the measured task position error $\tilde{\boldsymbol{x}}_i = \boldsymbol{x}_i - \boldsymbol{x}_{i,\mathrm{des}}(t)$. The Euclidean norm $\|\tilde{\boldsymbol{x}}_i\|$ as well as its root mean square

[1]The neck of Justin has two actuated joints, but they are not equipped with joint torque sensors and only provide a position control interface.

[2]Without loss of generality, we assume that $\boldsymbol{f}_i$ is continuously differentiable in $\boldsymbol{q}$, and $\boldsymbol{J}_i(\boldsymbol{q})$ is uniformly bounded in $\boldsymbol{q}$.

(RMS) value $\sqrt{\frac{1}{N}\sum_{k=1}^{N}\|\tilde{\boldsymbol{x}}_i(t_k)\|^2}$ over a time horizon of N time steps, are used as the quantitative measures.

- *Physical interaction*: The controlled robot is operated in trajectory tracking mode, but physical and artificial[3] interactions are applied across the task hierarchy, as illustrated in Fig. 1 (right). The interactive behavior of the system during the transient is analyzed by comparing the actual task position errors with the expected task deviations caused by external interactions. The latter quantities are determined through the assigned impedance on each hierarchy level.

III. Control Methods

A. Operational Space Formulation

The classical OSF approach [13], [24] fully compensates for the nonlinearities in (1) via feedback linearization, in order to enforce linear and decoupled closed-loop dynamics in task space. For the purpose of interaction control, this linear dynamics is mostly characterized by a desired mechanical impedance, which can be simulated as a mass-spring-damper system. The control law of OSF can be expressed as

$$\boldsymbol{\tau} = \boldsymbol{g} + \boldsymbol{C}\dot{\boldsymbol{q}} - \boldsymbol{\tau}^{\mathrm{ext}} + \boldsymbol{M}\boldsymbol{J}^{-1}(\ddot{\boldsymbol{x}}_{\mathrm{ref}} - \dot{\boldsymbol{J}}\dot{\boldsymbol{q}}) \ . \tag{8}$$

The impedance-based reference acceleration $\ddot{\boldsymbol{x}}_{\mathrm{ref}}$ is given by

$$\ddot{\boldsymbol{x}}_{\mathrm{ref}} = \ddot{\boldsymbol{x}}_{\mathrm{des}} + \boldsymbol{\Lambda}_{\mathrm{des}}^{-1}(\boldsymbol{F}_{\dot{\boldsymbol{x}}}^{\mathrm{ext}} - \boldsymbol{D}\dot{\tilde{\boldsymbol{x}}} - \boldsymbol{K}\tilde{\boldsymbol{x}}) \ , \tag{9}$$

in which $\dot{\tilde{\boldsymbol{x}}} = \dot{\boldsymbol{x}} - \dot{\boldsymbol{x}}_{\mathrm{des}}(t)$ denotes the task-space velocity error. Since OSF actively shapes the natural task-space inertia $\boldsymbol{\Lambda}$ towards a constant desired value $\boldsymbol{\Lambda}_{\mathrm{des}} = \mathrm{diag}\{\boldsymbol{\Lambda}_{i,\mathrm{des}}\}$, it requires the feedback of generalized external forces. The overall desired stiffness and damping in task space are described by $\boldsymbol{K} = \mathrm{diag}\{\boldsymbol{K}_i\}$ and $\boldsymbol{D} = \mathrm{diag}\{\boldsymbol{D}_i\}$, respectively. All submatrices $\boldsymbol{\Lambda}_{i,\mathrm{des}}, \boldsymbol{K}_i, \boldsymbol{D}_i \in \mathbb{R}^{m_i \times m_i}$ are supposed to be positive definite. Applying (8)–(9) to (1) results in the reference closed-loop dynamics $\ddot{\boldsymbol{x}} = \ddot{\boldsymbol{x}}_{\mathrm{ref}}$, which provides for each task a decoupled and exponential error convergence rate in free motion, and the desired impedance in response to interaction forces/torques.

B. Hierarchical PD+ Controller

To cope with the trajectory tracking problem, the HPD+ method [18] extends the hierarchical regulation controller [16], [17] with feedforward terms, in a similar manner as the joint-space PD+/augmented PD controller [25]. It preserves the natural inertial dynamics of the system, i. e. , no inertia shaping is involved, and it does not necessitate the feedback of external forces/torques. The HPD+ control law can be described as

$$\boldsymbol{\tau} = \boldsymbol{g} + \boldsymbol{\tau}_{\boldsymbol{\mu}} + \boldsymbol{\tau}_{\mathrm{pd}} + \boldsymbol{\tau}_{\mathrm{ff}} + \boldsymbol{\tau}_{\mathrm{comp}}^{\mathrm{ext}} \ , \tag{10a}$$

$$\boldsymbol{\tau}_{\boldsymbol{\mu}} = \bar{\boldsymbol{J}}^T(\boldsymbol{\mu} - \bar{\boldsymbol{\mu}})\boldsymbol{v} \ , \tag{10b}$$

$$\boldsymbol{\tau}_{\mathrm{pd}} = \bar{\boldsymbol{J}}^T(-\boldsymbol{D}\dot{\tilde{\boldsymbol{x}}} - \boldsymbol{K}\tilde{\boldsymbol{x}}) \ , \tag{10c}$$

$$\boldsymbol{\tau}_{\mathrm{ff}} = \bar{\boldsymbol{J}}^T(\boldsymbol{\Lambda}(\boldsymbol{B}\ddot{\boldsymbol{x}}_{\mathrm{des}} + \dot{\boldsymbol{B}}\dot{\boldsymbol{x}}_{\mathrm{des}}) + \bar{\boldsymbol{\mu}}\boldsymbol{B}\dot{\boldsymbol{x}}_{\mathrm{des}}) \ , \tag{10d}$$

$$\boldsymbol{\tau}_{\mathrm{comp}}^{\mathrm{ext}} = \bar{\boldsymbol{J}}^T(\boldsymbol{I} - \boldsymbol{B}^{-T})\boldsymbol{F}_{\dot{\boldsymbol{x}}}^{\mathrm{ext}} \ , \tag{10e}$$

[3]An artificial external torque/force is generated by additional motor commands, which are unknown to the controller.

where $\boldsymbol{B} = \bar{\boldsymbol{J}}\boldsymbol{J}^{-1} \in \mathbb{R}^{n\times n}$. The term $\boldsymbol{\tau}_{\boldsymbol{\mu}}$ compensates for the task-space Coriolis/centrifugal cross-couplings, and $\bar{\boldsymbol{\mu}}$ denotes the block diagonal part of $\boldsymbol{\mu}$. Note that $\boldsymbol{\tau}_{\boldsymbol{\mu}}$ does not lead to any power transmission between the controller and the robot due to the skew symmetry of $\dot{\boldsymbol{\Lambda}} - 2\bar{\boldsymbol{\mu}}$ [15]. The proportional derivative (PD) control action is described by $\boldsymbol{\tau}_{\mathrm{pd}}$, and $\boldsymbol{\tau}_{\mathrm{ff}}$ incorporates the feedforward terms. The *optional* term $\boldsymbol{\tau}_{\mathrm{comp}}^{\mathrm{ext}}$ cancels the cross-couplings in task-space external forces/torques, as will be explained. Applying (10) to (7) yields the closed-loop dynamics

$$\begin{aligned}\boldsymbol{\Lambda}\ddot{\tilde{\boldsymbol{x}}} + (\bar{\boldsymbol{\mu}} + \boldsymbol{D})\dot{\tilde{\boldsymbol{x}}} + \boldsymbol{K}\tilde{\boldsymbol{x}} = \boldsymbol{F}_{\dot{\boldsymbol{x}}}^{\mathrm{ext}} - \bar{\boldsymbol{\mu}}(\boldsymbol{B} - \boldsymbol{I})\dot{\tilde{\boldsymbol{x}}} \\ - \boldsymbol{\Lambda}((\boldsymbol{B} - \boldsymbol{I})\ddot{\tilde{\boldsymbol{x}}} + \dot{\boldsymbol{B}}\dot{\tilde{\boldsymbol{x}}}) \ ,\end{aligned} \tag{11}$$

where $\ddot{\tilde{\boldsymbol{x}}} = \ddot{\boldsymbol{x}} - \ddot{\boldsymbol{x}}_{\mathrm{des}}(t)$ denotes the task-space acceleration error. The closed loop (11) features uniform asymptotic stability of the origin $\tilde{\boldsymbol{x}} = \dot{\tilde{\boldsymbol{x}}} = \boldsymbol{0}$ in free motion, for which a formal proof can be found in [18]. Note that if $\boldsymbol{\tau}_{\mathrm{comp}}^{\mathrm{ext}}$ is not used due to the lack of measurement/estimation of $\boldsymbol{F}_{\dot{\boldsymbol{x}}}^{\mathrm{ext}}$, $\boldsymbol{B}^{-T}\boldsymbol{F}_{\dot{\boldsymbol{x}}}^{\mathrm{ext}}$ will appear as the first term on the right-hand side of (11), indicating the *bottom-up* couplings of generalized task-space external forces. This stems from the fact that $\boldsymbol{B}$ is a lower triangular matrix and correspondingly, $\boldsymbol{B}^{-T}$ is upper triangular, with their diagonal blocks being identity matrices [18]. The last two terms in (11) describe the *top-down* couplings complying with the dynamic consistency, such that tracking errors of any higher-priority tasks can impede the transient performance of a lower-priority task, but not vice versa. In the following, the control law of HPD+ without external force feedback, that is, without the use of (10e), will be denoted by HPD+$_{\text{w/o eff}}$, and the one with (10e) by HPD+$_{\text{w/ eff}}$, respectively.

C. Passive Decoupled Multi-Task Controller

Similar to OSF, the PDMT approach performs a full decoupling of the closed-loop dynamics using external force feedback, while preserving the nonlinear natural inertia as in HPD+. The decoupling at the kinematic level is achieved by modifying the feedforward terms in (10d) as

$$\begin{aligned}\boldsymbol{\tau}_{\mathrm{ff,pdmt}} = \bar{\boldsymbol{J}}^T\boldsymbol{\Lambda}(\ddot{\boldsymbol{x}}_{\mathrm{des}} + (\boldsymbol{B} - \boldsymbol{I})\ddot{\boldsymbol{x}}_{\mathrm{ref,pdmt}} + \dot{\boldsymbol{B}}\dot{\boldsymbol{x}}) \\ + \bar{\boldsymbol{J}}^T\bar{\boldsymbol{\mu}}(\dot{\boldsymbol{x}}_{\mathrm{des}} + (\boldsymbol{B} - \boldsymbol{I})\dot{\boldsymbol{x}}) \ ,\end{aligned} \tag{12}$$

where the reference acceleration is defined as (cf. (9))

$$\ddot{\boldsymbol{x}}_{\mathrm{ref,pdmt}} = \ddot{\boldsymbol{x}}_{\mathrm{des}} + \boldsymbol{\Lambda}^{-1}(\boldsymbol{F}_{\dot{\boldsymbol{x}}}^{\mathrm{ext}} - (\bar{\boldsymbol{\mu}} + \boldsymbol{D})\dot{\tilde{\boldsymbol{x}}} - \boldsymbol{K}\tilde{\boldsymbol{x}}) \ . \tag{13}$$

On the other hand, the bottom-up couplings in $\boldsymbol{B}^{-T}\boldsymbol{F}_{\dot{\boldsymbol{x}}}^{\mathrm{ext}}$ are compensated for as in HPD+$_{\text{w/ eff}}$. Note that the external force feedback used in PDMT aims at improving the interaction behavior of the robot, instead of shaping the natural inertia as in OSF. The resulting control law of PDMT is given by

$$\boldsymbol{\tau} = \boldsymbol{g} + \boldsymbol{\tau}_{\boldsymbol{\mu}} + \boldsymbol{\tau}_{\mathrm{pd}} + \boldsymbol{\tau}_{\mathrm{ff,pdmt}} + \boldsymbol{\tau}_{\mathrm{comp}}^{\mathrm{ext}} \ , \tag{14}$$

which leads to the closed-loop dynamics (cf. (11))

$$\boldsymbol{\Lambda}\ddot{\tilde{\boldsymbol{x}}} + (\bar{\boldsymbol{\mu}} + \boldsymbol{D})\dot{\tilde{\boldsymbol{x}}} + \boldsymbol{K}\tilde{\boldsymbol{x}} = \boldsymbol{F}_{\dot{\boldsymbol{x}}}^{\mathrm{ext}} \ . \tag{15}$$

In [19] it has been proven that (15) achieves uniform exponential stability of the origin and input-to-state stability under bounded external disturbances.

TABLE I

CONTROL GAINS FOR THE EXPERIMENTS

Gain	Experiments #1	Experiments #2
$\boldsymbol{K}_1, \boldsymbol{D}_1$	diag((900, 900, 900) $\frac{\text{N}}{\text{m}}$, (150, 150, 150) $\frac{\text{Nm}}{\text{rad}}$) / $\zeta = 0.7^{\star}$	diag((200, 200, 200) $\frac{\text{N}}{\text{m}}$, (50, 50, 50) $\frac{\text{Nm}}{\text{rad}}$) / $\zeta = 0.7$
$\boldsymbol{K}_2, \boldsymbol{D}_2$	diag((900, 900, 900) $\frac{\text{N}}{\text{m}}$, (150, 150, 150) $\frac{\text{Nm}}{\text{rad}}$) / $\zeta = 0.7$	diag((400, 400, 400) $\frac{\text{N}}{\text{m}}$, (100, 100, 100) $\frac{\text{Nm}}{\text{rad}}$) / $\zeta = 0.7$
$\boldsymbol{K}_3, \boldsymbol{D}_3$	diag((1200, 1200) $\frac{\text{N}}{\text{m}}$, 150 $\frac{\text{Nm}}{\text{rad}}$) / $\zeta = 0.7$	diag((1200, 1200) $\frac{\text{N}}{\text{m}}$, 100 $\frac{\text{Nm}}{\text{rad}}$) / $\zeta = 0.7$
$\boldsymbol{K}_4, \boldsymbol{D}_4$	diag((150, 150) $\frac{\text{Nm}}{\text{rad}}$) / diag((20, 20) $\frac{\text{Nms}}{\text{rad}}$)	diag((100, 100) $\frac{\text{Nm}}{\text{rad}}$) / diag((20, 20) $\frac{\text{Nms}}{\text{rad}}$)

* The damping ratio ζ is realized using the double diagonalization technique [26].

TABLE II

EXPERIMENTS #1: RMS ABSOLUTE TASK ERRORS

Lvl.	HPD+$_{\text{w/o eff}}$	HPD+$_{\text{w/ eff}}$	PDMT	OSF
L1 pos. [m]	**0.0054**	0.0083	0.0085	0.0074
L1 ang. [rad]	0.0105	0.0108	0.0107	0.0128
L2 pos. [m]	**0.0095**	0.0107	0.0107	0.0101
L2 ang. [rad]	**0.0096**	0.0104	0.0104	0.0119
L3 pos. [m]	0.0207	0.0193	**0.0182**	0.0199
L3 ang. [rad]	0.0351	0.0366	0.0371	0.0347
L4 [rad]	0.0269	0.0286	0.0215	**0.0200**

IV. EXPERIMENTS AND RESULTS

The controllers discussed in Section III, including both cases of the HPD+ control scheme, have been implemented on the upper body of Justin for experimental comparisons. The designed task hierarchy consists of four priority levels, as shown in Fig. 1 (left). Two sets of experiments are carried out according to the two application scenarios described in Section II-C. The applied control parameters are reported in Table I. Note that on levels 1-3 the implementation of damping ratios rather than constant damping matrices is intentionally designed for a more fair comparison, since the OSF approach results in different closed-loop inertial properties than the other approaches. In the physical interaction experiments (Experiments #2), low stiffness values are chosen for the tasks influenced by interactions/contacts, in order to obtain compliant interactive behaviors, while these values are still sufficient to drive the task coordinates back to their desired trajectories. For the OSF approach, the desired task-space inertia $\boldsymbol{\Lambda}_{\text{des}}$ is selected as the diagonal part of the natural inertia $\boldsymbol{\Lambda}$ in the initial configuration shown in Fig. 1 (left). The external torques applied on the entire upper body of the robot are estimated by using the classical momentum-based observer[4] [28], [29]. These quantities are transformed into task space via (4) for external force feedback required by the HPD+$_{\text{w/ eff}}$, PDMT, and OSF approaches.

A. Experiments #1: Tracking Performance in Free Motion

Fast and smooth sinusoidal/trapezoidal trajectories are commanded asynchronously on all hierarchy levels, as shown in Fig. 2. The maximum linear velocity achieved at the right TCP is about $0.34\,\text{m/s}$, and at the left TCP about $0.3\,\text{m/s}$. In Fig. 3, the task position errors with different controllers

[4]The observer gain is selected as $25\,\text{s}^{-1}$ for all joints, which is within the common range of $25\,\text{s}^{-1}$ to $75\,\text{s}^{-1}$ [27].

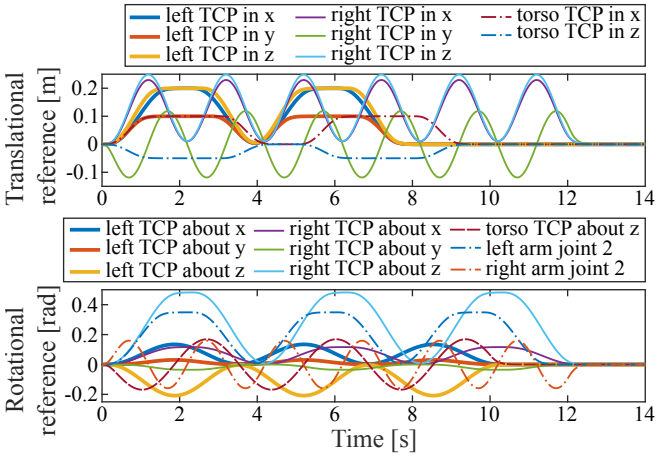

Fig. 2. Experiments #1: Reference trajectories of all tasks. Top: translational trajectories; Bottom: rotational trajectories. The desired orientation at each TCP is described by the Euler angels in the sequence x-y-z.

are compared. The RMS absolute errors are reported in Table II, where the values in bold indicate the superior performance of the respective controller, when it features a RMS tracking error that is at least 5% smaller than with any other controller in the specific task. As can be observed, HPD+$_{\text{w/o eff}}$ leads to the best performance on levels 1 and 2, although both PDMT and OSF should be able to show superior performance due to their proved exponential stability in theory. The worse performance of PDMT compared to HPD+$_{\text{w/o eff}}$ on these two levels is most likely attributed to the imperfect external force estimation by the momentum-based observer in practice, since PDMT results in similar transient response as HPD+$_{\text{w/ eff}}$, which only performs the external force decoupling in addition to HPD+$_{\text{w/o eff}}$. Note that the observer itself relies on an accurate dynamic model of the robot and thus, it can be corrupted by parameter variations or unmodeled dynamics, especially during fast motion. Moreover, in view of the upper triangular structure of $\boldsymbol{B}^{-T}$, an erroneous decoupling of $\boldsymbol{B}^{-T}\boldsymbol{F}_{\dot{\boldsymbol{x}}}^{\text{ext}}$ would significantly deteriorate performance on higher-priority levels. Besides the estimation errors of external force feedback, OSF can also suffer from the active inertia shaping under modeling errors. However, it is interesting to notice that OSF shows better performance than PDMT in the Cartesian position tasks at each TCP, but worse performance in the Cartesian orientation tasks on the same levels. This might be traced back to the configuration-dependent scaling of the feedback gains caused by inertia shaping [30], such that an increase of

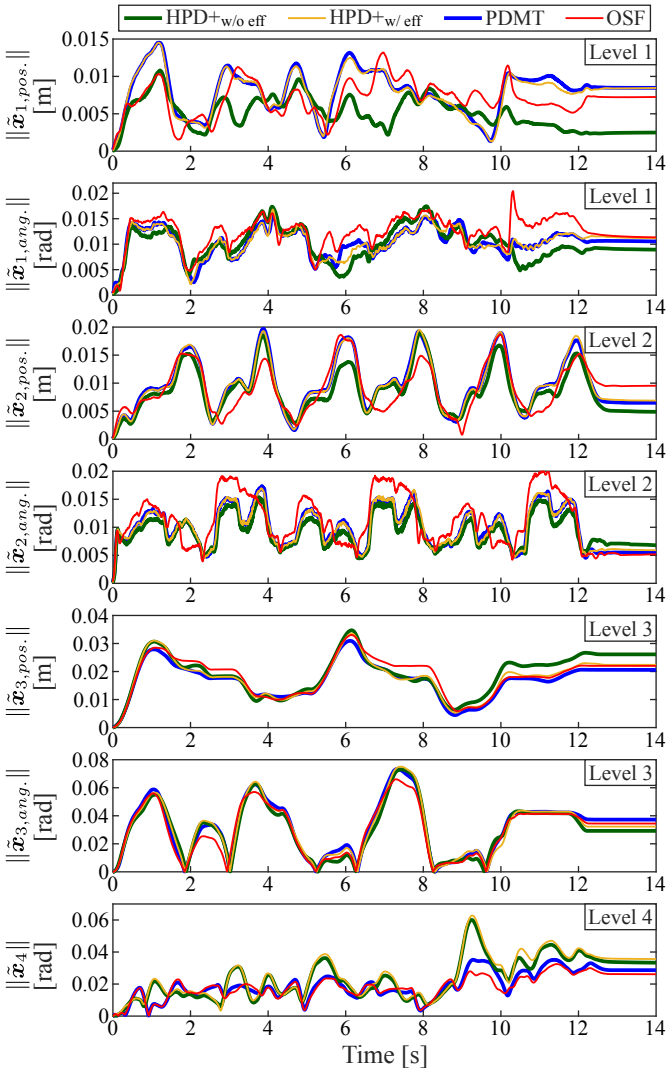

Fig. 3. Experiments #1: Euclidean norms of task position errors on all hierarchy levels. The notations $\|\tilde{\boldsymbol{x}}_{i,pos}\|$ and $\|\tilde{\boldsymbol{x}}_{i,ang}\|$ refer to the norms of the linear and angular components of $\tilde{\boldsymbol{x}}_i$, respectively. The orientation error at each TCP (diagrams 2 and 4) is represented by the absolute angle between the actual and the desired orientation of the TCP.

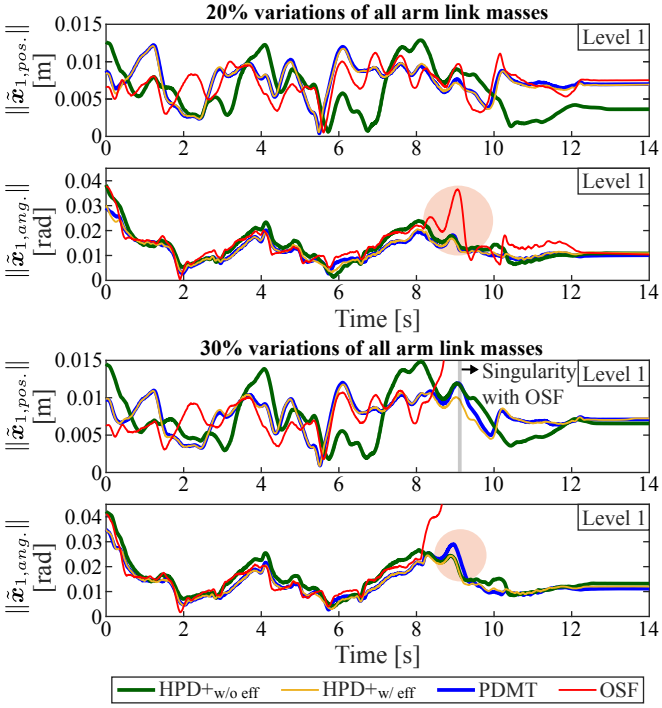

Fig. 4. Experiments #1: Euclidean norms of task position errors on level 1. The mass parameters of all arm links are randomly increased or reduced by 20% (diagrams 1 and 2) and 30% (diagrams 3 and 4), respectively.

TABLE III
EXPERIMENTS #1: RMS ABSOLUTE TASK ERRORS
(WITH 20% VARIATIONS OF ALL ARM LINK MASSES)

Lvl.	HPD+$_{\text{w/o eff}}$	HPD+$_{\text{w/ eff}}$	PDMT	OSF
L1 pos. [m]	**0.0067**	0.0075	0.0076	0.0073
L1 ang. [rad]	0.0144	0.0127	0.0126	0.0157
L2 pos. [m]	**0.0099**	0.0120	0.0120	0.0117
L2 ang. [rad]	**0.0106**	0.0122	0.0122	0.0143
L3 pos. [m]	0.0369	0.0357	0.0346	0.0382
L3 ang. [rad]	0.0342	0.0358	0.0369	0.0357
L4 [rad]	0.0274	0.0274	0.0211	**0.0200**

feedback gains, i. e. , stiffness and damping, could counteract the effects of modeling errors in dynamic compensation. On the lowest priority level, OSF and PDMT outperform both HPD+ approaches, which shows their effective compensation for the top-down kinematic couplings on this level.

In order to further investigate the influences of modeling errors on the controllers, the mass parameters of all fourteen arm links are randomly reduced or increased by 20% and 30% of their nominal values, respectively. Only the tracking errors on level 1 are illustrated in Fig. 4. The transient responses of the controllers on all other levels are comparable[5] to the case without parameter variations presented in Fig. 3. Note that due to corrupted gravity compensation, there remain considerable steady-state errors after initialization, but their influences on the overall transient responses are minimal. Table III catalogs the RMS absolute errors on all hierarchy levels under 20% mass parameter variations. As highlighted (red) in Fig. 4 (diagram 2), OSF results in significantly larger tracking errors in the Cartesian orientation task on level 1 under 20% parameter variations. The reasons might be two-fold: a) inertia shaping can contribute to performance degeneration in the presence of substantial modeling errors; b) a temporary task conflict between levels 1 and 4 can be induced by the sudden changes of the motion on level 4 (see Fig. 2 (bottom)). In comparison, a noticeable performance degradation of PDMT in the similar configuration only arises under 30% parameter variations, as highlighted in Fig. 4 (diagram 4). The performances of both HPD+ approaches are only slightly deteriorated by increased parameter variations, indicating their high robustness against model uncertainties. Moreover, with OSF the robot encounters kinematic singularity during left arm motion in the case of 30% parameter variations. This is mainly caused by the

[5]Except for the case with 30% mass parameter variations, in which OSF leads to singularity on level 1, as will be shown.

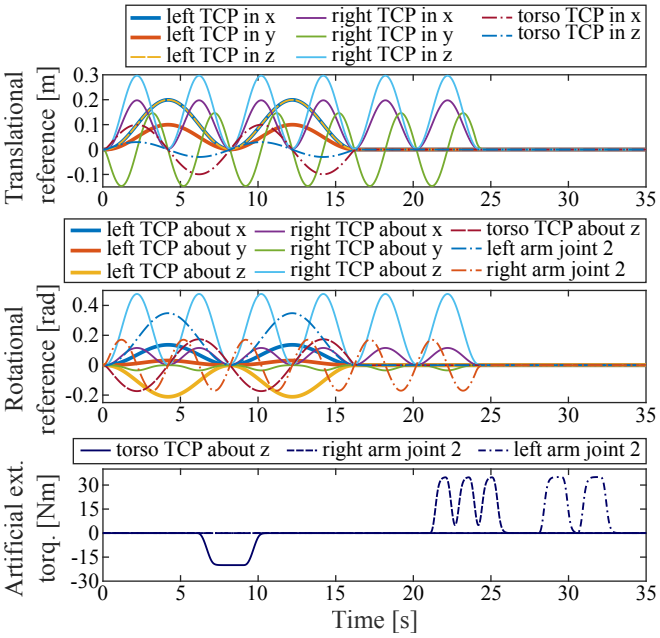

Fig. 5. Experiments #2: Reference trajectories (top and middle) and applied artificial external torques (bottom).

overcompensation for the gravity torques exerted on the torso joints, such that the torso moves upward excessively, reducing the overall manipulability of the arms. Nevertheless, with all other controllers the robot does not experience any singularity throughout the experiments.

B. Experiments #2: Interactive Behavior under Multiple Contacts and Interactions

For this set of experiments, slow reference trajectories, as presented in Fig. 5 (top and middle), are applied in order to better observe and assess the interactive behavior of the robot. Multiple interaction/contact conditions are designed for the experiments, as illustrated in Fig. 1 (right). To allow a reproducible physical contact with the environment, a foam cube attached to an unmovable table is placed in front of the left TCP (level 1). On the first joint of the torso (level 3) an artificial external torque of $-20\,\mathrm{Nm}$ is generated using motor commands. Similarly, artificial external torques of $35\,\mathrm{Nm}$ are exerted on the second joints of both arms (level 4). The applied artificial external torques are shown in Fig. 5 (bottom). Moreover, the right TCP (level 2) is grasped by a human and deviated from its desired trajectory between $t = 17{\sim}20\,\mathrm{s}$. In Fig. 6, the actual task errors and the expected task deviations under interaction forces/torques are depicted. The expected deviation for each task is obtained through the estimated generalized external force and the assigned stiffness, based on the desired impedance in quasi-static case (i. e. , $\dot{\tilde{\boldsymbol{x}}} = \ddot{\tilde{\boldsymbol{x}}} = \mathbf{0}$):

$$\text{expected deviation: } \tilde{\boldsymbol{x}}_i = \boldsymbol{K}_i^{-1} \boldsymbol{F}_{\dot{\boldsymbol{x}}_i}^{\text{ext}} \ ,$$

which is justified by the use of slow reference trajectories. As highlighted (cyan) in Fig. 6 (column 1), the desired interaction response of HPD+$_{\text{w/o eff}}$ is severely affected by the bottom-up couplings in $\boldsymbol{B}^{-T}\boldsymbol{F}_{\dot{\boldsymbol{x}}}^{\text{ext}}$, while HPD+$_{\text{w/ eff}}$ and PDMT can successfully compensate for such couplings, despite the imperfect external force feedback. For example, the artificial external torque applied to the second joint of the left arm (level 4) during $t = 28{\sim}33\,\mathrm{s}$ induces the largest position errors on level 1 using HPD+$_{\text{w/o eff}}$. The overall interaction behaviors of HPD+$_{\text{w/ eff}}$ and PDMT are comparable on all hierarchy levels, only on the lowest level PDMT leads to slightly better performance, as seen from the last row in Fig. 6. Compared with HPD+$_{\text{w/ eff}}$ and PDMT, the active inertia shaping of OSF results in worse external force decoupling on level 1, as highlighted in Fig. 6 (column 4). To demonstrate the performed inertia shaping of OSF more clearly, the diagonal terms $\boldsymbol{\Lambda}_1(k,k)$ and $\boldsymbol{\Lambda}_{1,\text{des}}(k,k)$ for $k = 1 \ldots 6$ are depicted in Fig. 7. Note that the occurrences of deteriorated interaction response of OSF coincide with the dramatic changes of the natural inertia. This indicates that instantaneous inertia variations cannot be adequately compensated for via feedback actions in practice. The snapshots in Fig. 8 further illustrate the comparisons of the interactive behaviors with different controllers on level 1.

V. Discussion

A qualitative characterization of the controllers in terms of their general properties is illustrated in Fig. 9. Since OSF not only cancels the cross-couplings among the hierarchy levels but also actively shapes the nonlinear natural inertia, it involves the most task-space decoupling actions. In comparison, PDMT preserves the natural inertia on each level as both HPD+ approaches, and it only compensates for the task-space couplings across the hierarchy border: top-down couplings in kinematic quantities and bottom-up couplings in generalized external forces. Similar to PDMT, HPD+$_{\text{w/ eff}}$ also counteracts the bottom-up couplings using external force feedback, while HPD+$_{\text{w/o eff}}$ keeps the minimum amount of task-space decoupling: inherited inertial decoupling by null-space projection and power-conserving Coriolis/centrifugal decoupling. On the other hand, the model-based dynamic compensation is known to be sensitive to parameter variations or unmodeled dynamics. Moreover, the external force feedback can also contribute to a lower robustness of the closed-loop system due to unavoidable measurement noises or estimation errors in practice.

Nevertheless, in both sets of conducted experiments, the external force feedback appeared to be unproblematic if the natural inertia was preserved. Despite considerable estimation errors of the momentum-based observer, both HPD+$_{\text{w/ eff}}$ and PDMT performed well in Experiments #1. Indeed, without the feedback decoupling of generalized external forces, HPD+$_{\text{w/o eff}}$ was not able to retain the desired impedance on higher-priority levels in the presence of external interactions on lower-priority levels, as seen in Experiments #2. Only when external force feedback was adopted together with active inertia shaping, as in OSF, significant performance deterioration or even instability was observed under model uncertainties. The practical difference between HPD+$_{\text{w/ eff}}$ and PDMT was minimal in general, except on the lowest

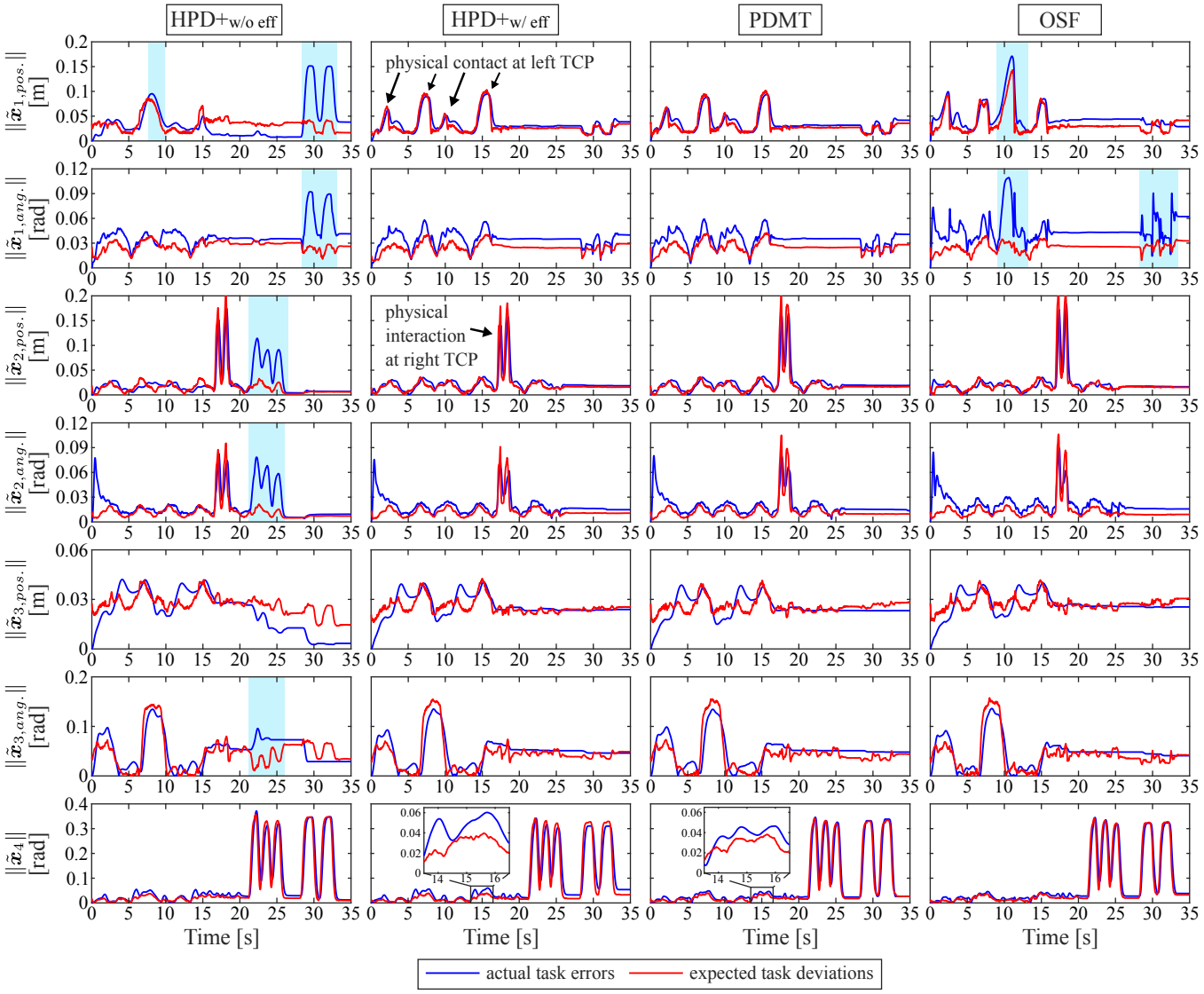

Fig. 6. Experiments #2: Euclidean norms of the actual task errors and of the expected trajectory deviations in the presence of external interactions.

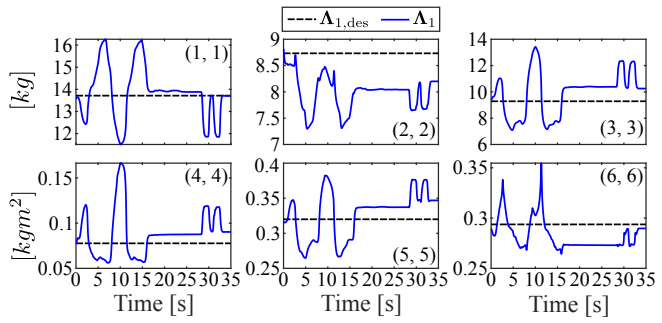

Fig. 7. Experiments #2: All six diagonal terms of the desired inertia used in OSF (black dashed) and those of the natural inertia (blue) on level 1.

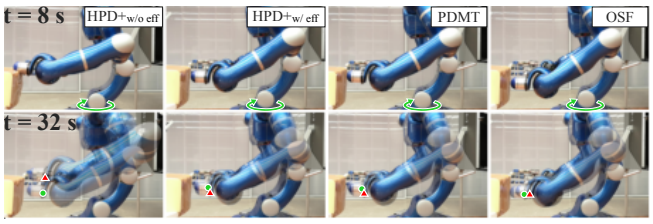

Fig. 8. Experiments #2: Snapshots of the left TCP positions in x-z plane. Top: with HPD+$_{\text{w/o eff}}$ the external torque on level 3 (curved green arrow) disturbs the task execution on level 1, causing the left TCP to stay in contact with the environment. Bottom: with HPD+$_{\text{w/o eff}}$ the actual position (red triangle) of the left TCP significantly deviates from its steady state (green dot) in the presence of the external torque on level 4. The steady-state TCP positions are acquired via snapshots at $t = 27$ s.

level where the top-down couplings compensation by PDMT led to marginally better performance.

VI. Conclusion

In this paper, experimental comparisons of three multi-tasking control strategies including both alternatives of HPD+ without/with external force feedback, namely OSF, HPD+$_{\text{w/o eff}}$, HPD+$_{\text{w/ eff}}$, and PDMT, were demonstrated on the humanoid system Justin, with a focus on their tracking performance in free motion and interactive behavior under physical interaction. In theory, OSF and PDMT feature uniform exponential stability for trajectory tracking, while

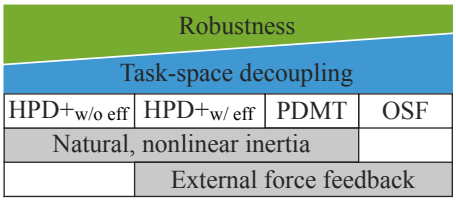

Fig. 9. Qualitative characterization of different controllers.

both HPD+ approaches only allows the proof of uniform asymptotic stability. However, our study revealed that OSF and PDMT only outperformed the HPD+ control scheme on the lowest priority level in practice, while HPD+$_{\text{w/o eff}}$ led to superior performance on higher-priority levels. The approaches avoiding inertia shaping, that is, PDMT and both versions of HPD+, showed high robustness against model uncertainties. Under large dynamic parameter variations, OSF could lead to instability or unexpected singularity in undisturbed motions. When the robot had multiple physical contacts/interactions across the hierarchy, PDMT and HPD+$_{\text{w/ eff}}$ gave rise to less corrupted interactive behavior prescribed by the desired impedance, compared to both HPD+$_{\text{w/o eff}}$ and OSF.

REFERENCES

[1] A. Dietrich, T. Wimböck, A. Albu-Schäffer, and G. Hirzinger, "Reactive whole-body control: Dynamic mobile manipulation using a large number of actuated degrees of freedom," *IEEE Robotics & Automation Magazine*, vol. 19, no. 2, pp. 20–33, June 2012.

[2] J. Lim, I. Lee, I. Shim, H. Jung, H. M. Joe, H. Bae, O. Sim, J. Oh, T. Jung, S. Shin, K. Joo, M. Kim, K. Lee, Y. Bok, D.-G. Choi, B. Cho, S. Kim, J. Heo, I. Kim, J. Lee, I. S. Kwon, and J.-H. Oh, "Robot system of DRC-HUBO+ and control strategy of team KAIST in DARPA robotics challenge finals," *Journal of Field Robotics*, vol. 34, no. 4, pp. 802–829, 2017.

[3] N. Kashiri, L. Baccelliere, L. Muratore, A. Laurenzi, Z. Ren, E. M. Hoffman, M. Kamedula, G. F. Rigano, J. Malzahn, S. Cordasco, P. Guria, A. Margan, and N. G. Tsagarakis, "Centauro: A hybrid locomotion and high power resilient manipulation platform," *IEEE Robotics and Automation Letters*, vol. 4, no. 2, pp. 1595–1602, 2019.

[4] D. Leidner, A. Dietrich, M. Beetz, and A. Albu-Schäffer, "Knowledge-enabled parameterization of whole-body control strategies for compliant service robots," *Autonomous Robots*, vol. 40, no. 3, pp. 519–536, March 2016.

[5] L. Saab, O. E. Ramos, F. Keith, N. Mansard, P. Souères, and J.-I. Fourquet, "Dynamic whole-body motion generation under rigid contacts and other unilateral constraints," *IEEE Transactions on Robotics*, vol. 29, no. 2, pp. 346–362, April 2013.

[6] A. Herzog, N. Rotella, S. Mason, F. Grimminger, S. Schaal, and L. Righetti, "Momentum control with hierarchical inverse dynamics on a torque-controlled humanoid," *Autonomous Robots*, vol. 40, no. 3, pp. 473–491, March 2016.

[7] K. Bouyarmane and A. Kheddar, "On weight-prioritized multitask control of humanoid robots," *IEEE Transactions on Automatic Control*, vol. 63, no. 6, pp. 1632–1647, June 2018.

[8] Y. Nakamura, H. Hanafusa, and T. Yoshikawa, "Task-priority based redundancy control of robot manipulators," *International Journal of Robotics Research*, vol. 6, no. 2, pp. 3–15, June 1987.

[9] B. Siciliano and J.-J. Slotine, "A general framework for managing multiple tasks in highly redundant robotic systems," in *Proc. of the 5th International Conference on Advanced Robotics*, June 1991, pp. 1211–1216.

[10] O. Khatib, "Inertial properties in robotic manipulation: An object-level framework," *International Journal of Robotics Research*, vol. 14, no. 1, pp. 19–36, February 1995.

[11] ——, "A unified approach for motion and force control of robot manipulators: The operational space formulation," *IEEE Journal of Robotics and Automation*, vol. RA-3, no. 1, pp. 43–53, February 1987.

[12] L. Sentis and O. Khatib, "Prioritized multi-objective dynamics and control of robots in human environments," in *4th IEEE/RAS International Conference on Humanoid Robots, 2004.*, vol. 2, Nov 2004, pp. 764–780.

[13] L. Sentis and O. Khatib, "Synthesis of whole-body behaviors through hierarchical control of behavioral primitives," *International Journal of Humanoid Robotics*, vol. 2, no. 4, pp. 505–518, January 2005.

[14] P. H. Chang and J. W. Jeong, "Enhanced operational space formulation for multiple tasks by using time-delay estimation," *IEEE Transactions on Robotics*, vol. 28, no. 4, pp. 773–786, 2012.

[15] C. Ott, A. Kugi, and Y. Nakamura, "Resolving the problem of non-integrability of nullspace velocities for compliance control of redundant manipulators by using semi-definite Lyapunov functions," in *Proc. of the 2008 IEEE International Conference on Robotics and Automation*, May 2008, pp. 1999–2004.

[16] A. Dietrich, C. Ott, and A. Albu-Schäffer, "Multi-objective compliance control of redundant manipulators: Hierarchy, control, and stability," in *Proc. of the 2013 IEEE/RSJ International Conference on Intelligent Robots and Systems*, November 2013, pp. 3043–3050.

[17] C. Ott, A. Dietrich, and A. Albu-Schäffer, "Prioritized multi-task compliance control of redundant manipulators," *Automatica*, vol. 53, pp. 416–423, March 2015.

[18] A. Dietrich and C. Ott, "Hierarchical impedance-based tracking control of kinematically redundant robots," *IEEE Transactions on Robotics*, vol. 36, no. 1, pp. 204–221, February 2020.

[19] X. Wu, C. Ott, A. Albu-Schäffer, and A. Dietrich, "Passive decoupled multi-task controller for redundant robots," *IEEE Transactions on Control Systems Technology*, 2022.

[20] A. Dietrich, M. Kimmel, T. Wimböck, S. Hirche, and A. Albu-Schäffer, "Workspace analysis for a kinematically coupled torso of a torque controlled humanoid robot," in *Proc. of the 2014 IEEE International Conference on Robotics and Automation*, June 2014, pp. 3439–3445.

[21] R. Ortega and M. W. Spong, "Adaptive motion control of rigid robots: A tutorial," *Automatica*, vol. 25, pp. 877–888, 1989.

[22] S. R. Ploen, "A skew-symmetric form of the recursive Newton-Euler algorithm for the control of multibody systems," *Proceedings of the 1999 American Control Conference*, vol. 6, pp. 3770–3773 vol.6, 1999.

[23] P. Baerlocher and R. Boulic, "Task-priority formulations for the kinematic control of highly redundant articulated structures," in *Proc. of the 1998 IEEE/RSJ International Conference on Intelligent Robots and Systems*, October 1998, pp. 323–329.

[24] O. Khatib, L. Sentis, J. Park, and J. Warren, "Whole-body dynamic behavior and control of human-like robots," *International Journal of Humanoid Robotics*, vol. 1, no. 1, pp. 29–43, March 2004.

[25] B. Paden and R. Panja, "Globally asymptotically stable PD+ controller for robot manipulators," *International Journal of Control*, vol. 47, no. 6, pp. 1697–1712, 1988.

[26] A. Albu-Schäffer, C. Ott, U. Frese, and G. Hirzinger, "Cartesian impedance control of redundant robots: Recent results with the DLR-light-weight-arms," in *Proc. of the 2003 IEEE International Conference on Robotics and Automation*, September 2003, pp. 3704–3709.

[27] S. Haddadin, A. De Luca, and A. Albu-Schäffer, "Robot collisions: A survey on detection, isolation, and identification," *IEEE Transactions on Robotics*, vol. 33, no. 6, pp. 1292–1312, December 2017.

[28] A. de Luca and R. Mattone, "Sensorless robot collision detection and hybrid force/motion control," in *Proceedings of the 2005 IEEE International Conference on Robotics and Automation*, 2005, pp. 999–1004.

[29] A. De Luca, A. Albu-Schaffer, S. Haddadin, and G. Hirzinger, "Collision detection and safe reaction with the DLR-III lightweight manipulator arm," in *2006 IEEE/RSJ International Conference on Intelligent Robots and Systems*, Oct 2006, pp. 1623–1630.

[30] A. Dietrich, X. Wu, K. Bussmann, M. Harder, M. Iskandar, J. Englsberger, C. Ott, and A. Albu-Schäffer, "Practical consequences of inertia shaping for interaction and tracking in robot control," *Control Engineering Practice*, vol. 114, p. 104875, 2021.